Single excitatory axons form clustered synapses onto CA1 pyramidal cell dendrites

Erik B. Bloss [ID], Mark S. Cembrowski, Bill Karsh, Jennifer Colonell, Richard D. Fetter and Nelson Spruston [ID]*

CA1 pyramidal neurons are a major output of the hippocampus and encode features of experience that constitute episodic memories. Feature-selective firing of these neurons results from the dendritic integration of inputs from multiple brain regions. While it is known that synchronous activation of spatially clustered inputs can contribute to firing through the generation of dendritic spikes, there is no established mechanism for spatiotemporal synaptic clustering. Here we show that single presynaptic axons form multiple, spatially clustered inputs onto the distal, but not proximal, dendrites of CA1 pyramidal neurons. These compound connections exhibit ultrastructural features indicative of strong synapses and occur much more commonly in entorhinal than in thalamic afferents. Computational simulations revealed that compound connections depolarize dendrites in a biophysically efficient manner, owing to their inherent spatiotemporal clustering. Our results suggest that distinct afferent projections use different connectivity motifs that differentially contribute to dendritic integration.

Hippocampal area CA1 is part of the medial temporal lobe system, which underlies the formation, maintenance and plasticity of episodic memories[1,2]. The encoding of higher order associative features by CA1 pyramidal cells results from spatial and contextual representations within afferent projections from the entorhinal cortex (EC) and midline thalamus[3–6], as well as from area CA3 via the transformation of EC input through the hippocampal trisynaptic loop[7–9].

The ability of these functionally distinct excitatory projections to drive action potential output in CA1 pyramidal cells is influenced by their stringent spatial organization onto distinct dendritic compartments. Intrahippocampal projections from area CA3 target the basal dendrites in stratum oriens and proximal apical dendrites in stratum radiatum (SR), while long-range, extrahippocampal EC and midline thalamus inputs target the distal apical tuft dendrites in stratum lacunosum-moleculare (SLM). The more distal location of SLM synapses places strong biophysical constraints on their ability to drive action potential output[10,11]. Their influence at the soma is further decreased by their reduced expression of glutamate receptors compared to SR synapses[12].

To overcome the distance-dependent filtering properties of the dendritic cable, excitatory synapses in SLM might contribute to action potential output through the preferential recruitment of local dendritic excitability[13,14]. The presence of active dendritic conductances enables dendrites to selectively amplify synaptic activity through the generation of sodium or calcium spikes[15]. These dendritic events are facilitated by spatially and temporally correlated synaptic input patterns[16–18], which has inspired models in which clustered sets of coactive excitatory synapses are the physical substrate of memory storage in CA1 pyramidal cells[19,20]. Intriguingly, recent experiments have demonstrated spatial clusters of synchronously active excitatory synapses on hippocampal neurons in vitro[21,22] and on neocortical pyramidal neurons in vivo[23,24] (however, see ref. [25,26]).

These experiments visualized activity in postsynaptic structures, but remarkably little is known about the axonal wiring patterns that might support these functional synaptic clusters. A simple way this

input structure could be achieved is by single axons forming multiple, spatially localized connections onto the same dendritic branch. Previous reports have found instances of this form of connectivity[27–32], but the extent, identity and specificity with which afferent circuits utilize this connectivity motif remains unclear.

Here we show that long-range excitatory inputs to SLM dendrites, but not intrahippocampal inputs to SR dendrites, show a surprisingly high density of spatially clustered synapses consisting of a single axon forming multiple connections onto spines belonging to the same parent dendrite; we call these "compound synapses." These synapses have distinct pre- and postsynaptic features and are formed differentially among cortical and thalamic afferent projections. Computational simulations demonstrate that this simple wiring motif efficiently drives dendritic depolarization and promotes the summation of coactivated synapses. Taken together, these results suggest a set of projection-specific wiring rules that govern the functional clustering of excitatory synaptic connections.

Results

Classification of excitatory axonal connectivity onto CA1 dendrites by ssTEM. We reasoned that the simplest implementation of a wiring scheme that could produce spatially clustered, temporally synchronous and functionally related synaptic activity would entail individual excitatory axons making multiple, closely spaced synaptic contacts onto their target dendrites. To search for these connections, we used serial section transmission electron microscopy (ssTEM) to image a tissue volume ($350\,\mu m \times 200\,\mu m \times 17\,\mu m$; spatial resolution of $3.8\,nm/pixel$, section thickness of $50\,nm$) containing SR and SLM of hippocampal area CA1 (Fig. 1a and Supplementary Video 1).

Excitatory synapses could be identified easily by the presence a postsynaptic density (PSD) in the electron micrographs, and they were readily differentiated from symmetric, inhibitory synapses (Fig. 1a and Supplementary Fig. 1a). We reconstructed dendritic segments and their associated dendritic spines from SR (located approximately 80–100 μm from the SR–SLM border; $n = 8$ segments, $27.2 \pm 3\,\mu m$ in length) and from SLM (located approximately

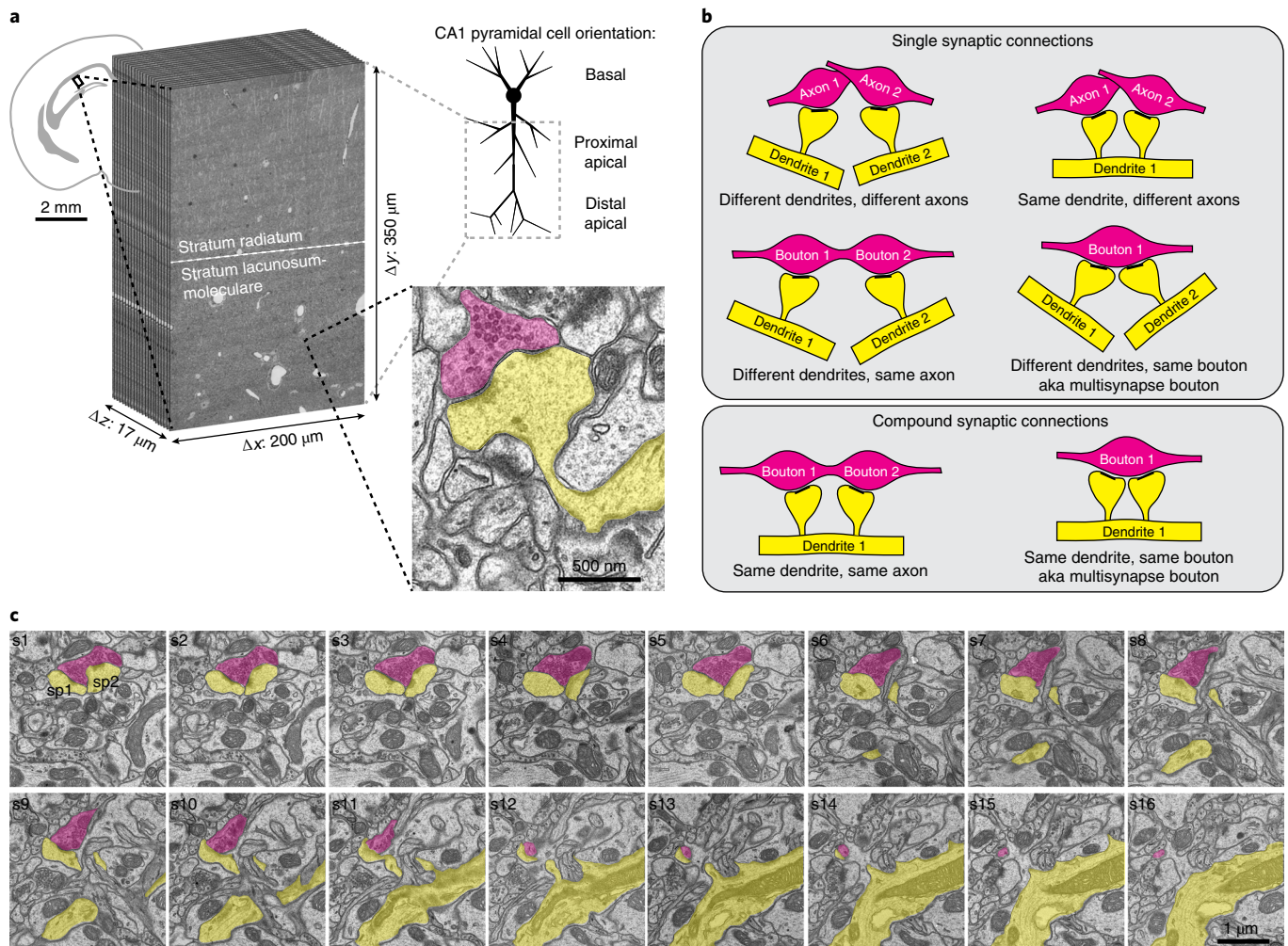Howard Hughes Medical Institute, Janelia Research Campus, Ashburn, VA, USA. *e-mail: sprustonn@janelia.hhmi.org

Fig. 1 | Classification of single-axon connectivity by serial section transmission electron microscopy. a, The location, dimensions and representative synaptic ultrastructure (presynaptic, magenta; postsynaptic, yellow) from the electron microscopy volume used in the present study ($n = 1$ imaged volume). **b**, Possible configurations of excitatory connectivity between individual axons (magenta) and their target dendrites (yellow). Top, potential arrangements of single synaptic connections. Bottom, the potential configurations of compound synaptic connections (i.e., multiple synaptic connections between the same axon and the same dendrite). **c**, Serial sections (s1–s16) of an excitatory axon (magenta) forming a compound synaptic connection onto a pair of neighboring spines (sp1 and sp2, yellow) that arise from the same parent dendrite (example from $n = 72$ observed compound connections). See Supplementary Fig. 1 and Supplementary Video 1 for additional data.

80–100 μm past the SR–SLM border; $n = 12$ segments, 27.5 ± 3 μm in length) and analyzed every excitatory synapse formed onto each segment (total of 969 synaptic connections, Supplementary Fig. 1b–d). For each excitatory synapse identified, we followed its axon to determine whether the axon formed another synapse on the same dendritic segment; if subsequent synapses were identified, this set of synapses was classified as compound while all other synapses were classified as single (Fig. 1b,c).

Compound synaptic connectivity is selective for apical tuft dendrites of CA1 pyramidal cells. Reconstructions of pyramidal cell dendritic segments from SR (Fig. 2a and Supplementary Fig. 2a) revealed that virtually all afferent excitatory connections were made by individual axons forming a synapse onto a single dendritic spine and that the occurrence of multiple spines belonging to the same dendrite and sharing a common axon was rare (compound: ~1% of all synapses; Fig. 2a,b and Supplementary Fig. 2a,b). These data are consistent with previous reports showing a low occurrence of compound synapses on dendrites in SR of area CA1 in the rat[28,29,31].

By contrast, compound synapses were much more frequent on pyramidal cell dendrites in SLM (compound: ~25% of all synapses; Fig. 2a,b and Supplementary Fig. 2a,b). The higher proportion of compound synapses on tuft branches was not simply due to the lower overall synaptic density on these dendrites, as the numbers of afferent axons making compound synapses scaled more steeply with the total number of afferent axons on SLM than SR branches (Fig. 2b). Moreover, the density of compound synapses was significantly higher on SLM dendrites despite the large decrease in spine density between SR and SLM branches (Supplementary Fig. 2b).

Axonal path lengths and angular trajectories relative to their target dendrite differed slightly between SR and SLM axons (SR, $n = 259$; SLM, $n = 152$; Supplementary Fig. 2c), suggesting that the rate of compound connectivity could result from differences in axonal geometry. However, individual synapses within a compound connection were tightly clustered at a spatial scale well below the traceable path length (mean intersynapse distance, 2.0 ± 0.2 μm, all <8 μm apart, Fig. 2c; mean axon path length: SR, 16.7 ± 0.5 μm; SLM, 18.3 ± 0.6 μm; Supplementary Fig. 2c). Moreover, neither
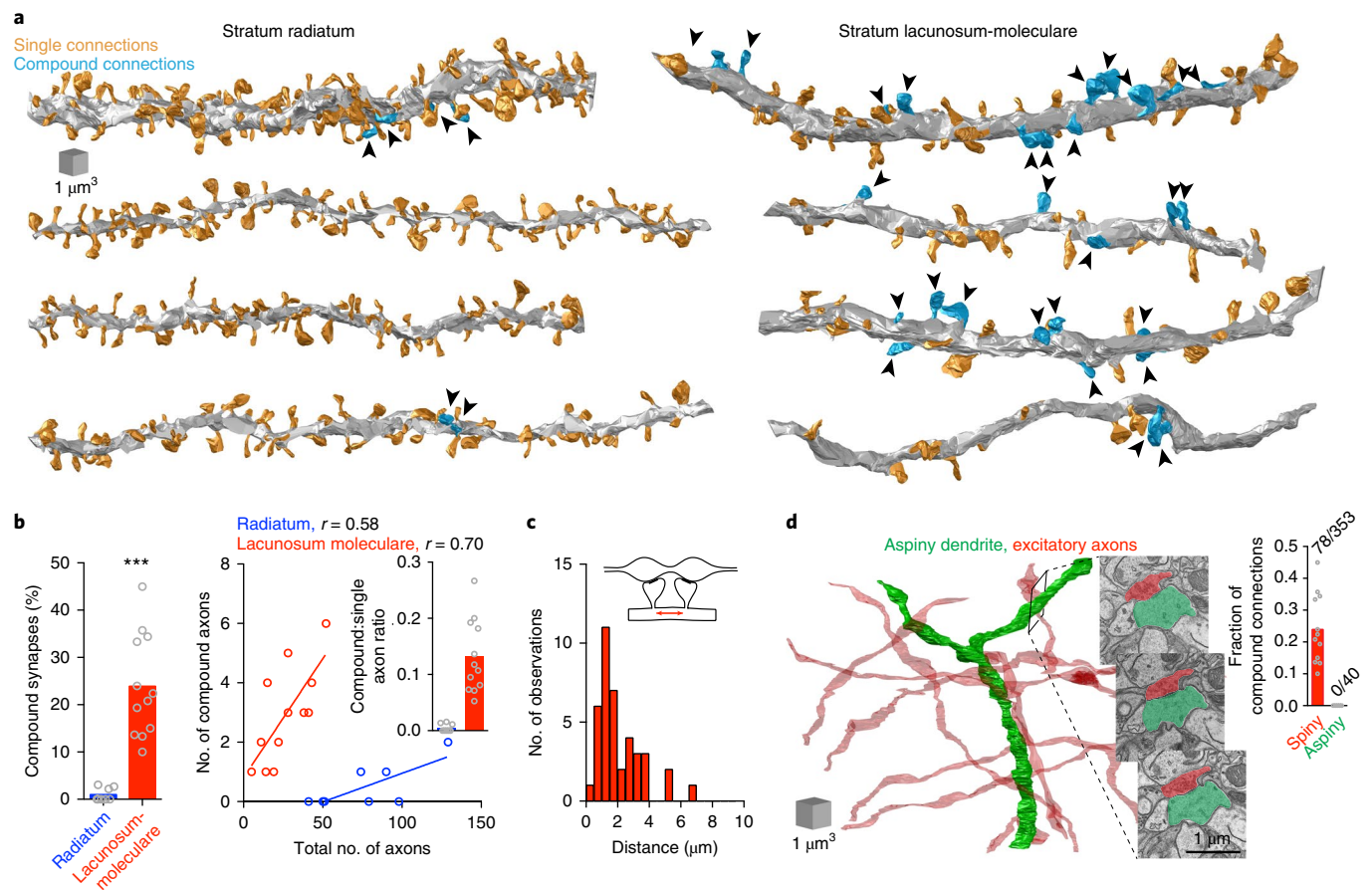
Fig. 2 | Differential occurrence of compound synapses in area CA1. a, Examples of reconstructed dendritic branch segments and their associated spines from SR (left, $n=8$ independent SR branch segments and $n=616$ reconstructed spines) and SLM (right, $n=12$ independent SLM branch segments and $n=322$ reconstructed spines). Single synaptic connections are rendered orange and compound synaptic connections are rendered blue and marked by arrowheads. Compound synapses made onto the dendritic shaft are not indicated. Scale cube applies to both sets of dendrites. **b**, The prevalence of compound synapses differs between pyramidal cell dendrites from SR (blue, $n=8$ independent reconstructed segments) and SLM (red, $n=12$ independent reconstructed segments). Left, the percentage of synapses belonging to compound synapses (two-sided Mann–Whitney test, ***$P<0.0001$). Right, the relationship between the number of axons making compound synaptic connections and the total number of axons making synaptic connections onto each branch (two-sided Spearman correlations: SR, $r=0.58$, $P=0.14$; SLM: $r=0.70$, $P=0.01$; difference between best-fit slopes, $P=0.02$). Inset, the ratio of axons making compound synapses to axons making single synapses. **c**, The distribution of intersynapse distances between individual spines belonging to compound synapses on SLM branches ($n=40$ compound spine pairs; mean, 2.1 μm). **d**, Compound synapses were absent on putative interneuron dendrites in SLM. Left, an example reconstruction of an aspiny, putative interneuron dendrite (green) and its presynaptic excitatory axons (red) (example from $n=5$ reconstructed aspiny dendrites). Right, three serial micrographs through an axodendritic excitatory synapse ($n=40$ reconstructed asymmetric synapses on aspiny dendrites). No compound synapses were found on aspiny dendrites (inset: $n=12$ reconstructed SLM pyramidal cell dendritic segments and $n=5$ aspiny dendritic segments, two-sided Fisher's exact test, $P<0.0001$). See Supplementary Fig. 2 for additional data.

the path length nor angular trajectory differed between axons forming single or compound connections in SLM (Supplementary Fig. 2d). Finally, even when we restricted our analysis to axons with long path lengths (>20 μm) or crossing their target dendrites at more acute angles (<40°), large differences in the rate of compound connections remained evident between SR and SLM (data not shown). These results strongly suggest the differential occurrence of compound connections between SR and SLM is independent of axonal geometry.

The ultrastructural features of SLM compound connections varied, but were predominantly pairs (86%) rather than triplets or quadruplets, were predominantly made onto dendritic spines (85%) rather than a mix of spines and dendritic shafts or shafts only, and predominantly formed by separate synaptic boutons (74%) rather than on the same bouton (Supplementary Fig. 2e). The number of synapses comprising each compound connection was 2.1 ± 0.06, and segments often had multiple sets of compound connections

(3.0 ± 0.46 per segment; see Supplementary Fig. 2a). To discriminate whether compound connections were a general feature of excitatory connectivity within SLM or specifically targeted to the dendrites of pyramidal cells, we examined excitatory connectivity onto aspiny, putative interneuron dendrites in SLM (Fig. 2d, $n=5$, 22.7 ± 3 μm in length). No compound connections were found on these branches (Fig. 2d, $P<0.0001$), strongly suggesting that this form of synaptic connectivity in SLM of CA1 is specific to pyramidal cell dendrites.

Compound synapses occur selectively at spines with distinct ultrastructural features. The ultrastructural features of dendritic spines are strong predictors of their functional properties, with larger spines associated with greater strength in vitro and greater stability in vivo[33]. Spine volumes and PSD areas were strongly correlated for both single and compound synapses in SLM ($n=195$ single and $n=56$ compound synapses; Fig. 3a). However, dendritic spines from compound connections had larger volumes and PSD

areas compared to single connections (Fig. 3b and Supplementary Fig. 3a). In contrast, spine neck diameters correlated poorly with spine volume or PSD area and did not differ between single and compound synapses (Supplementary Fig. 3b).

The configuration of the PSD is associated with distinct modes of glutamate receptor expression. Spine synapses in SLM with perforated PSDs (i.e., those containing one or more discontinuities; see Fig. 3c) are known to express 3- to 4-fold more AMPA
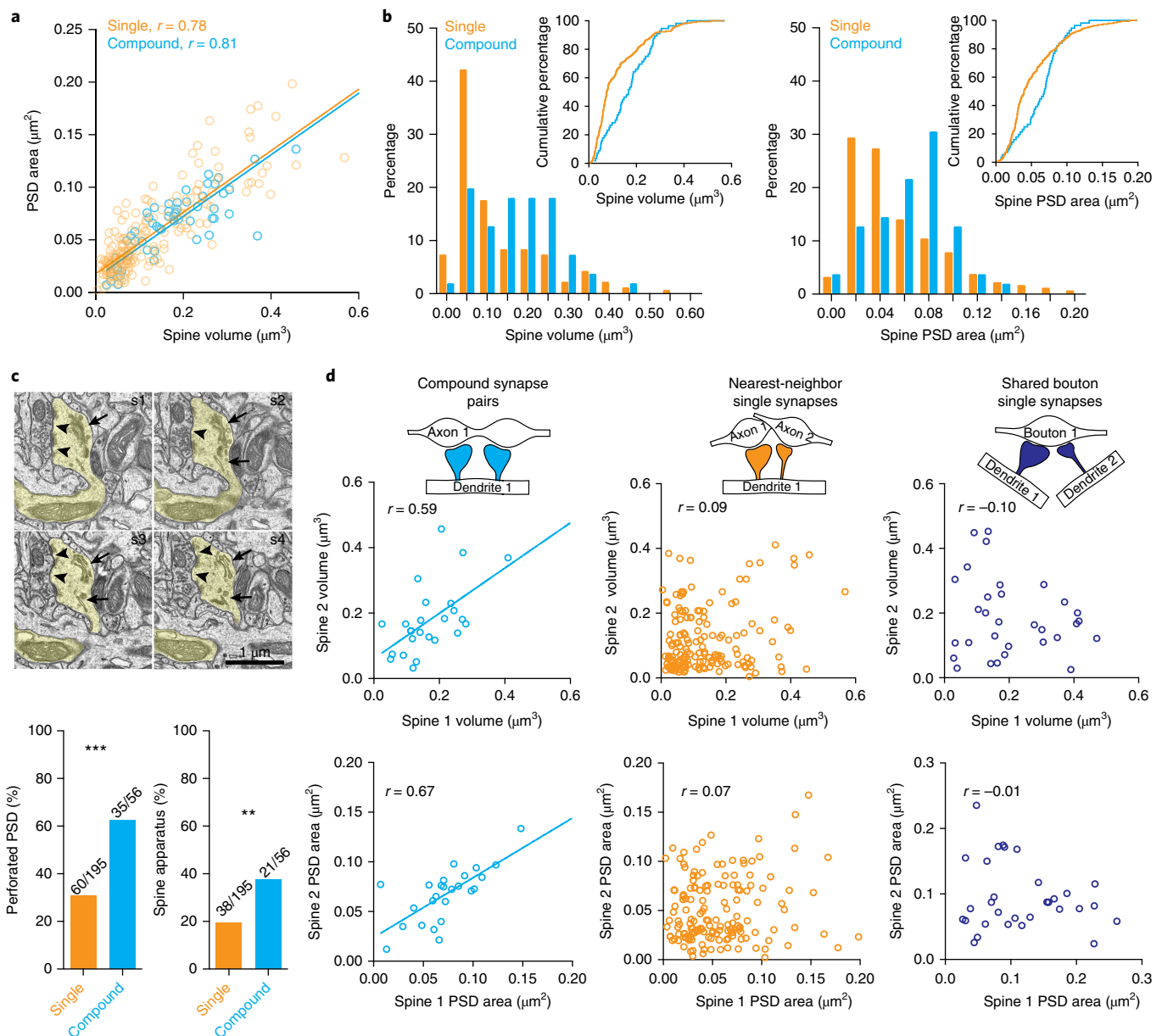

Fig. 3 | Ultrastructural features of dendritic spines from compound synapses. a, Correlation between spine volume and PSD area from dendritic spines belonging to single synapses (orange, $n = 195$ spine reconstructions) and compound synapses (blue, from $n = 56$ spine reconstructions) in SLM (two-sided Spearman correlation: single; $r = 0.78$, $P < 0.0001$; compound; $r = 0.81$, $P < 0.0001$; difference between best-fit slopes, $P = 0.2$). **b**, Dendritic spine morphology from SLM single and compound synapses. Left, histogram showing the percentage of spine volumes from single (orange) and compound (blue) synapses (χ^2 test, $P = 0.003$). Inset, cumulative frequency plots ($P < 0.0001$, two-sided Kolmogorov–Smirnov test). Right, same but for PSD areas (χ^2 test, $P = 0.002$,). Inset, cumulative frequency plots (two-sided Kolmogorov–Smirnov test, $P < 0.0001$). **c**, Top, serial sections (s1–s4) through a dendritic spine (example from $n = 251$ reconstructed SLM spines) containing both a perforated PSD (arrowheads) and a spine apparatus (arrows). Bottom, the percentage of synapses that contain either a perforated PSD (left; two-sided Fisher's exact test, ***$P < 0.0001$) or a spine apparatus (right; two-sided Fisher's exact test, **$P = 0.007$) between single or compound spine synapses. **d**, Morphological correlations between SLM compound spine synapse pairs. Top row: left, spine volumes from pairs of compound synapses ($n = 25$ pairs; two-sided Spearman correlation, $r = 0.59$, $P = 0.001$). Center, spine volumes from pairs of nearest neighbor single synaptic connections ($n = 152$ pairs; two-sided Spearman correlation, $r = 0.09$, $P = 0.26$). Right, spine volumes from pairs of single synaptic connections that share the same presynaptic bouton ($n = 31$ pairs; two-sided Spearman correlation, $r = -0.10$, $P = 0.57$). Bottom row: same as top, but for PSD area (compound: $n = 25$ pairs, two-sided Spearman correlation, $r = 0.67$, $P = 0.0003$; nearest neighbors: $n = 152$ pairs, two-sided Spearman correlation, $r = 0.07$, $P = 0.39$; same presynaptic bouton: $n = = 31$ pairs, two-sided Spearman correlation, $r = -0.009$, $P = 0.95$). See Supplementary Fig. 3 for additional data.
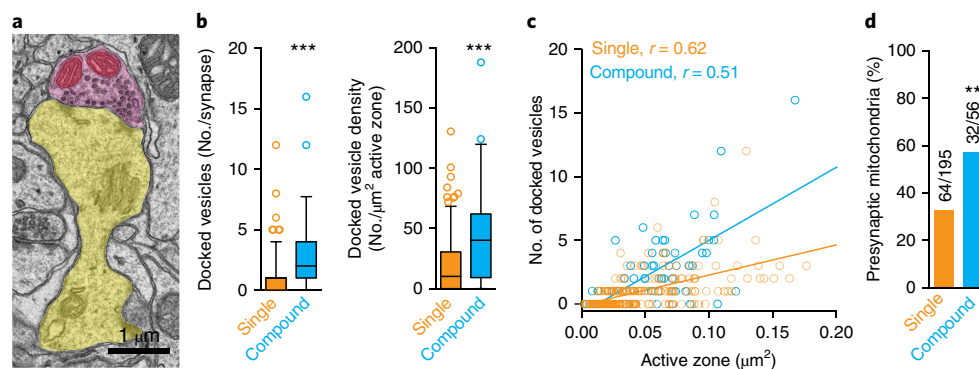
Fig. 4 | Presynaptic ultrastructure differs between single and compound synaptic connections. a, A representative axospinous synapse with the presynaptic axon shaded magenta, synaptic vesicles in darker magenta, presynaptic mitochondria in red, and postsynaptic spine and dendritic shaft in yellow (from $n = 251$ spine synapse reconstructions). **b**, Left, the number of docked synaptic vesicles differs between single (orange, $n = 195$) and compound synapses (blue, $n = 56$) (two-sided Mann–Whitney test, ***$P < 0.0001$); right, the density of docked vesicles differs between single and compound synapses (same synapses as on left; vesicle number per μm^2 of presynaptic active zone: two-sided Mann–Whitney test, ***$P < 0.0001$). In box and whisker plots, box depicts 25th percentile, median and 75th percentile and whiskers depict 5th to 95th percentiles; data points outside these ranges are shown as individual circles. **c**, The relationship between docked vesicle number and synaptic active zone size (single: $n = 195$, two-sided Spearman correlation, $r = 0.62$, $P < 0.0001$; compound: $n = 56$, two-sided Spearman correlation, $r = 0.51$, $P < 0.0001$; difference between best-fit slopes, extra sum-of-squares test, $P < 0.0001$). **d**, The percentage of SLM axospinous synapses containing presynaptic mitochondria from single or compound synapses (two-sided Fisher's exact test, **$P = 0.0016$). See Supplementary Fig. 4 for additional data.

receptors (AMPARs) and 50% more NMDA receptors (NMDARs) than SLM synapses with unperforated PSDs[12]. In our dataset, the percentage of spines from compound connections that contained perforated PSDs was more than twice as high as spines from single connections (62% of compound synapses vs. 30% of single connections) (Fig. 3c).

The spine apparatus is a spine-specific organelle that has been linked to calcium handling and synaptic plasticity[34]. The percentage of spines from compound connections that contained a spine apparatus was twice as high as in spines from single connections (38% of compound synapses vs. 19% of single synapses; Fig. 3c and Supplementary Fig. 3c,d). The presence of these two ultrastructural features provides additional evidence that compound synapses are a subset of strong and stable synapses in SLM.

Morphologies of spines belonging to a compound connection are correlated. Although spines from compound connections are larger as a population, we wondered whether there was any relationship between the individual spines that were associated with a compound connection. On the one hand, if the spines within a compound connection act as independent postsynaptic structures, then their volumes and PSD sizes should appear random relative to each other. On the other hand, the shared pre- and postsynaptic activity that are inherent to compound connections might produce spines with similar ultrastructural features[28].

When we examined spine pairs from compound connections, we found a significant positive correlation between their spine volumes ($n = 25$ pairs, $r = 0.59$) and between their PSD areas ($n = 25$ pairs, $r = 0.67$; Fig. 3d; although we note the strength of each correlation was notably lower than a recently report from compound connections in SR[28]). To determine whether this morphological relationship was restricted to compound connections, we examined the relationship between pairs of spine volumes and between pairs of PSD areas from two related sets of single connections. Neither nearest-neighbor single connection spines ($n = 152$ pairs) nor spines on different parent dendrites but connected to the same axonal bouton ($n = 31$ pairs) had correlated spine volumes or PSD areas (Fig. 3d). These data support the hypothesis that the shared pre- and postsynaptic activity of compound synapses imparts a strong influence on spine morphology on CA1 dendrites[28].

Presynaptic architecture differs between single and compound synapses. The efficacy of communication at a synapse is dependent not only on the postsynaptic sensitivity, but also on the probability and dynamics of synaptic vesicle release from the presynaptic terminal. Several presynaptic features, including the size of the presynaptic active zone and the number of docked synaptic vesicles, are ultrastructural correlates of release probability at hippocampal synapses[35].

When we examined presynaptic ultrastructure of SLM synapses (Fig. 4a), we found that the average number of docked synaptic vesicles (defined as vesicles with centers located within 25 nm of the active zone membrane) was approximately three times larger at compound synapses than for single synapses (Fig. 4b). Surprisingly, the average density of docked vesicles (normalized per μm^2 of active zone) was also significantly higher at compound synapses than at single synapses (Fig. 4b,c). Nearly identical results were obtained when the inclusion criterion for synaptic vesicles was increased from within 25 nm of the active zone to within 50 nm (Supplementary Fig. 4a,b).

Lastly, the presence of mitochondria in presynaptic terminals is known to influence local calcium handling and synaptic vesicle motility[36]. In our dataset, presynaptic mitochondria were associated with synapses containing larger active zones, greater numbers of docked vesicles per synapse and higher docked vesicle density (Supplementary Fig. 4c). The percentage of terminals that contained mitochondria at compound synapses was nearly twice that of single synapses (57% of compound synapses vs. 34% of single synapses; Fig. 4d). Taken together, these presynaptic features are consistent with an elevated probability of vesicle release at compound synapses compared to their single-synapse counterparts.

Axon segments that make compound connections preferentially use multisynapse boutons. The previous results demonstrate clear ultrastructural differences between single and compound synapses, but do not tell us whether the connectivity of axons forming compound synapses differs from those that only form single synapses on a larger scale. We examined this by reconstructing a set of SLM axon segments ($n = 43$; mean segment length, $25.5 \pm 1.9\,\mu m$) and classifying each as either a segment that formed single synapses only ($n = 18$) or a segment that formed at least one compound
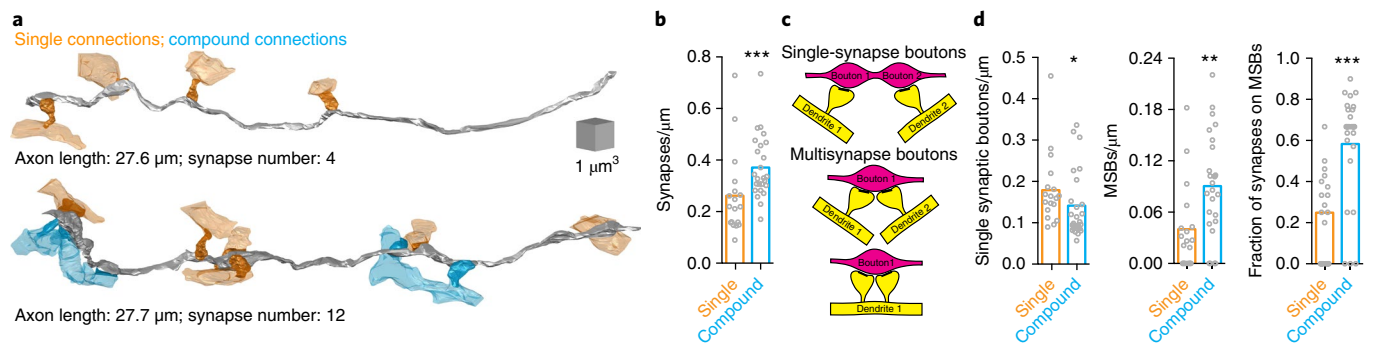
Fig. 5 | Local synaptic connectivity of axon segments making single or compound synapses. a, Example reconstructions of axon segments ($n = 43$ reconstructed axon segments; axon in gray, postsynaptic dendritic spines and shafts that form single synapses in orange, and postsynaptic dendritic spines and shafts that that form compound synapses in blue). Top, an axonal segment that made single synapses only. Bottom, an axonal segment that made three separate compound synapses. Scale cube applies to both axon reconstructions. **b**, The density of excitatory synapses along axon segments making single synapses only (orange, $n = 18$) or at least one compound synapse (blue, $n = 25$) (two-sided Mann–Whitney test, ***$P = 0.0004$). **c**, Configurations of single-synapse boutons and multisynapse boutons. Multisynaptic boutons can innervate multiple single synapses belonging to different dendrites or occur at compound synapses. **d**, Axon segments making compound connections (blue, $n = 25$) preferentially form multisynaptic boutons compared to axon segments making single connections only (orange, $n = 18$). Left, the density of single synapse boutons on axon segments (two-sided Mann–Whitney test, *$P = 0.02$). Center, the density of multisynaptic boutons (MSBs) on these same axon segments (two-sided Mann–Whitney test, **$P = 0.003$). Right, the fraction of all synapses that occur on MSBs from these same segments (two-sided Mann–Whitney test, ***$P < 0.0001$). See Supplementary Fig. 5 for additional data.

connection ($n = 25$) (Fig. 5a and Supplementary Fig. 5a,b). A subset of segments was identified in an unbiased manner using the dissector method ($n = 20$; see Methods), and 50% were found to make compound connections along the reconstructed segment length. For all reconstructed segments, we also examined the postsynaptic structures and were able to replicate the basic morphological features of compound synapses found in our dendrite-based dataset (Supplementary Fig. 5d).

Both sets of reconstructed axon segments predominantly formed axospinous synapses compared to axodendritic synapses (number of connections per segment: single, 6.1 ± 0.7 vs. 0.7 ± 0.2; compound, 7.2 ± 0.8 vs. 0.9 ± 0.2; Supplementary Fig. 5d). On segments that made compound connections, the mean number of synapses within each compound connection was 2.1 ± 0.07. Segments that made at least one compound connection had synaptic densities that were ~40% higher than segments making single connections only (Fig. 5b and Supplementary Fig. 5e,f). Furthermore, segments that made compound connections had more than twice the density of multisynaptic boutons (MSBs) (Fig. 5c,d) than those that only made single connections. When all synaptic connections were taken into account, more than half (58%) of synapses along segments forming compound connections were part of an MSB; in contrast, this fraction was less than 25% on axon segments forming single synapses only (Fig. 5d). Although we cannot determine whether all SLM axons make compound connections at some point along their length or whether there are two distinct axon types, these data provide evidence that axons forming local compound synapses show an elevated synapse density through the preferential formation of MSBs.

Occurrence of compound synapses depends on afferent projection identity. The ultrastructural differences in axons making single or compound connections suggested that they might arise from different afferent projections. The two main excitatory projections targeting pyramidal cell tuft dendrites arise from the medial EC (MEC) and the lateral EC (LEC). In addition, a sparser set of projections arises from neurons in the midline thalamus[37]. To examine the connectivity of individual axons from identified projections, we turned to array tomography (Fig. 6a)[38–40]. The advantages of this technique include sample compatibility with correlative light and

electron microscopy[40], subdiffraction resolution in the z axis, and the capacity for rapid and depth-independent imaging of fluorescent signals at submicron resolution across large volumes.

Neurons from the MEC, LEC and midline thalamus were engineered to express a cytoplasmic epitope tag by viral injections of viruses encoding Cre recombinase (AAV2/1-Cre) and a Cre-dependent V5 tag (AAV2/1-FLEX-rev-smRuby2_V5)[41] (Fig. 6b,c). When MEC synaptic connections were mapped onto the tuft dendrites of pyramidal cells, approximately 41% (77 of 187) were characterized as compound synapses (Fig. 6d,e). By contrast, 26% (39 of 152) of synapses made by LEC afferents were characterized as compound ($P = 0.002$, MEC vs. LEC), and only 3% (2 of 60) of synapses from midline thalamus were characterized as compound ($P < 0.0001$ for either MEC or LEC vs. midline thalamus). The percentages of MEC and LEC synapses that belong to compound connections compares favorably with our estimate of 25% from ssTEM (Fig. 2b).

We replicated these results with an additional set of arrays in which MEC or LEC axons were labeled via a retrograde strategy (i.e., injection of AAV2retro-Cre[42] into CA1 SLM followed by injection of AAV2/1-FLEX-rev-smRuby2_V5 into MEC or LEC; Supplementary Fig. 6a,b). In this pair of arrays, 38% (57 of 149) of MEC synapses were classified as compound compared to only 21% (14 of 66) of LEC synapses ($P = 0.018$, Supplementary Fig. 6c). Collectively, these findings show that a strong circuit-selective bias (MEC over LEC over midline thalamus) exists in the propensity to form compound synapses onto pyramidal cell tuft dendrites.

Projection selectivity of compound synapses is specific to EC layer III→CA1. Are compound synapses made by these EC projection neurons specific to CA1 dendrites, or are they a general feature of their connectivity? To gain restricted genetic access to the EC layer III population of neurons projecting to CA1 (ECIII→CA1), we took advantage of the observation that ECIII→CA1 neurons, but rarely EC layer II (ECII) neurons that project to the dentate gyrus, send their axons to the contralateral hippocampus (Fig. 7a and Supplementary Fig. 7a–c). Injections of AAVs encoding Cre-dependent fluorescent proteins into the ipsilateral MEC and LEC along with injections of AAV2retro-Cre into the contralateral CA1 SLM resulted in reporter expression in EC layer III neurons with
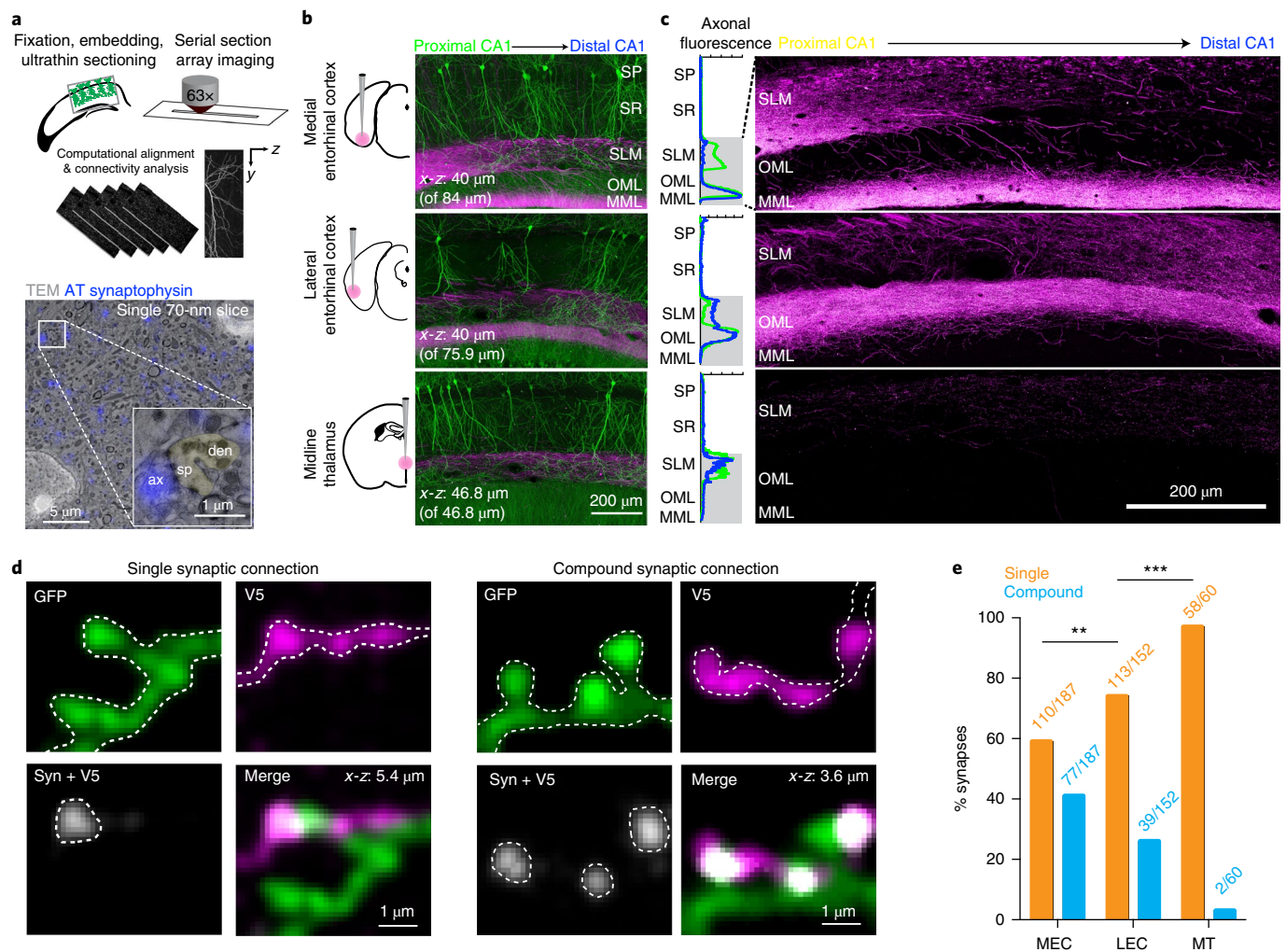
Fig. 6 | Projection-specific differences in the occurrence of compound synapses revealed by large-volume array tomography. a, Array tomography workflow. Top, samples from dorsal hippocampus of Thy-1 GFP-M transgenic mice were prepared for array tomography, imaged by light microscopy or by correlative light and electron microscopy, and computationally aligned for synaptic connectivity analysis. Bottom, a portion of a 70-nm slice with synaptophysin immunoreactivity (blue) and DAPI (gray) from light microscopy overlaid onto the TEM ultrastructure (from $n = 7$ serial slices). Inset, higher magnification image of synaptophysin immunoreactivity over the presynaptic vesicle population at an excitatory synapse (spine shaded green; ax, axon; sp, spine; den, dendrite). **b,** Large-scale analysis of excitatory afferent projections targeting the tuft dendrites of CA1 pyramidal cells. Maximum intensity projection of array tomography volumes ($n = 1$ large-volume array for each projection; 100-nm-thick serial sections) containing afferents labeled by virus injection into (from top to bottom) medial entorhinal cortex, lateral entorhinal cortex and midline thalamus. SP, stratum pyramidale; OML, outer molecular layer; MML, middle molecular layer. **c,** Axon gradients from afferent projections. Left, normalized axonal fluorescence from the proximal and distal portions of area CA1 and dentate gyrus for each projection ($n = 4$ or 5 regions of interest for proximal and distal from each array volume). Right, maximum intensity projections of the axon labeling (magenta) and colocalized synaptophysin puncta (gray) from the same array volumes as in **b**. **d,** Single and compound synapses on tuft dendrites (from $n = 399$ identified SLM synapses). Left, an example single connection consisting of a single axon contacting a single GFP+ spine (projection of 54 100-nm serial sections; from $n = 281$ identified single connections). Right, an example of a compound connection consisting of a single axon contacting three neighboring GFP+ spines (projection of 36 100-nm serial sections; from $n = 118$ identified compound synapses). **e,** The occurrence of compound connections varied significantly among afferent projections ($n = 187$ MEC synapses, $n = 152$ LEC synapses, and $n = 60$ midline thalamus synapses: two-sided Fisher's exact test, MEC vs. LEC, ***$P = 0.0028$; two-sided Fisher's exact test, LEC vs. midline thalamus, **$P < 0.0001$). See Supplementary Fig. 6 for additional data.

axonal projections largely restricted to CA1 SLM bilaterally within the hippocampus (Supplementary Fig. 7b,c). In addition, ECIII→CA1 neurons also sent a weaker axonal projection to the basolateral amygdala (BLA) (Fig. 7b).

We used array tomography to reconstruct the connectivity of V5-expressing ECIII→CA1 axons onto BLA excitatory neurons[43] from Thy-1 YFP-H mice (Fig. 7b). We found that ECIII connectivity in BLA differed strongly from that in CA1 in two ways. First, both sets of afferent projections rarely made compound synapses onto excitatory BLA neurons (as in Fig. 7c). Specifically, only 9%

(8 of 88) of medial ECIII→CA1 synaptic connections and 8% (6 of 75) of lateral ECIII→CA1 synaptic connections in BLA were classified as compound. The rate of compound synapses for each projection in BLA was significantly lower than their corresponding rate in CA1 ($P < 0.001$ for both). Second, the rate of compound synapses between the two afferent projections in the BLA was indistinguishable, whereas it differed strongly in area CA1. Thus, even within excitatory ECIII→CA1 projection neurons, the propensity to form compound synapses is highly dependent on the local synaptic target.
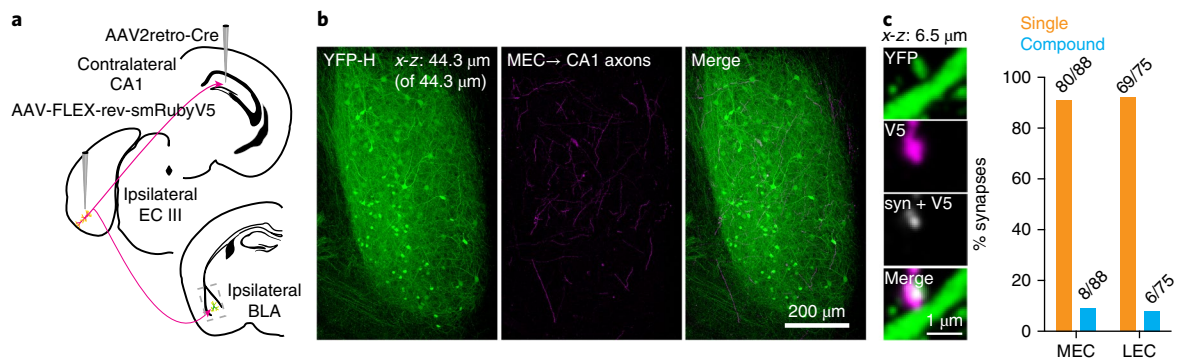
Fig. 7 | Medial and lateral entorhinal cortical layer III→CA1 projection neurons have similar rates of compound synapses in the basolateral amygdala. **a**, An AAV2retro-Cre strategy enables selective access to ECIII→CA1 neurons. Injection of AAV2retro-Cre into the contralateral CA1 region followed by injections of Cre-dependent constructs expressing epitope tag V5 into the ipsilateral EC selectively labeled CA1-projecting neurons (from $n=3$ animal replicates). **b**, Maximum intensity projection of an array tomography volume (from 100-nm-thick sections) containing YFP-expressing BLA neurons (green) and V5-expressing axons (magenta) from MECIII→CA1 neurons (from $n=1$ large-volume array for each projection). **c**, Left, an example single connection onto a spiny BLA neuron dendrite (from $n=163$ identified synapses on BLA neurons). Right, the prevalence of single and compound synapses onto BLA neurons was indistinguishable between MECIII→CA1 and LECIII→CA1 projections ($n=88$ MEC synapses, $n=75$ LEC synapses: two-sided Fisher's exact test, MEC vs. LEC, $P=1.0$). See Supplementary Fig. 7 for additional data.

Functional effects of compound connections. What are the functional effects of compound synaptic connections on CA1 pyramidal cells? Using a computational approach, we first asked what advantage, if any, is conferred by the presence of two separate synapses rather than one synapse with twice the excitatory synaptic conductance. We started with a simple model consisting of a soma and a single dendritic branch with passive biophysical properties. A pair of neighboring spine synapses containing AMPARs were placed halfway along the dendritic branch and three synapse configurations were compared: a single input made onto one spine ('single'), two inputs spread across the two neighboring spines ('compound synapse') and two inputs made onto one spine ('2×synapse') (Fig. 8a,b).

In all conditions, as expected, the spine head voltage was attenuated across the dendritic spine neck (resistance = 500 MΩ), producing a smaller voltage change in the parent dendrite[44]. The compound synapse configuration resulted in nearly perfect linear dendritic summation (i.e., peak voltage amplitudes in the parent dendrite that were equivalent to that of the single input scaled twofold). By contrast, the 2×synapse configuration produced peak voltage amplitudes that were approximately 27% smaller (Fig. 8a,b). The smaller dendritic depolarization in the 2×synapse configuration resulted from the decreased driving force at the synapse as a consequence of the larger spine head depolarization, thus reducing the total charge entry associated with synapse activation.

Nearly identical results were obtained from tuft synapses placed onto a more realistic CA1 pyramidal cell morphology[40] containing active dendritic conductances (i.e., voltage-gated Na+ and K+ channels) and excitatory synapses with both AMPARs and NMDARs. Specifically, for a synapse midway along the tuft, activation of synapses in the compound configuration resulted in a −3% deviation from linearity, while activation of a 2×synapse resulted in a −21% deviation from linearity (Fig. 8c,d). Generally, compound synapses produced approximately linear integration of synaptic inputs in parent dendrites (Fig. 8c), whereas larger sublinearities were evident in the 2×synapse configuration across the entire dendritic morphology (Fig. 8c,d and Supplementary Fig. 8a). For the 2× synapse configuration to produce a peak dendritic voltage equivalent to the scaled single input in the apical tuft, the synaptic conductance needed to be increased approximately threefold (Supplementary Fig. 8b). Lastly, compared to the 2×synapse configuration, a compound synapse pair always produced larger dendritic depolarizations

regardless of whether the pair was made onto two spines, one on a spine and one directly onto the dendritic shaft, or both directly onto the dendritic shaft (Supplementary Fig. 8c).

We next examined how the spatial and temporal features inherent to compound connections shaped local dendritic integration. In the simple model morphology, a dendritic spine synapse containing AMPARs was placed halfway along the branch length (Fig. 8e). For each simulation, the location (0–100% along the branch length) and temporal activation ($\Delta t; \pm 50$ ms relative to synapse 1) of a second dendritic spine synapse (synapse 2) was varied. At all dendritic locations for synapse 2, the peak local dendritic voltage was maximal when the temporal offset was within a few milliseconds. Similarly, in all simulations where $\Delta t = 0$, the peak local dendritic voltage change was maximal when synapse 2 was placed adjacent to synapse 1 (Fig. 8e).

This spatiotemporal pattern of summation was accentuated in the CA1 pyramidal cell model with active dendrites and both AMPARs and NMDARs (Fig. 8f). The maximal dendritic voltage change in the dendrite adjacent to synapse 1 occurred when the two synapses were clustered both in time and in space. Notably, when $\Delta t = 0$, the spatial pattern of synaptic input that produced the maximal dendritic depolarization was nearly identical to the empirically observed distribution of distances between synapses within a compound connection (Fig. 8f,g). Moreover, the suite of features associated with compound synapses (i.e., the occurrence of triplets and quadruplets, and their putative increased postsynaptic strength and presynaptic reliability) should all serve to enhance further the synaptic efficiency and synaptic summation of compound synapses relative to single synapses.

Discussion

The presence of functional clusters of excitatory synapses on individual dendritic branches has been hypothesized to serve as the physical substrate of learning and memory in models of CA1 pyramidal cells[19,20]. Remarkably little is known, however, about synaptic clustering from the perspective of axonal architecture. Here we show that a simple wiring motif—compound synapses—produces spatially clustered and functionally similar sets of excitatory synapses at high density on pyramidal cell dendrites in SLM. Array tomography revealed compound synapses are found differentially among cortical and thalamic afferent projections targeting tuft dendrites. Lastly, our computational simulations demonstrated that the
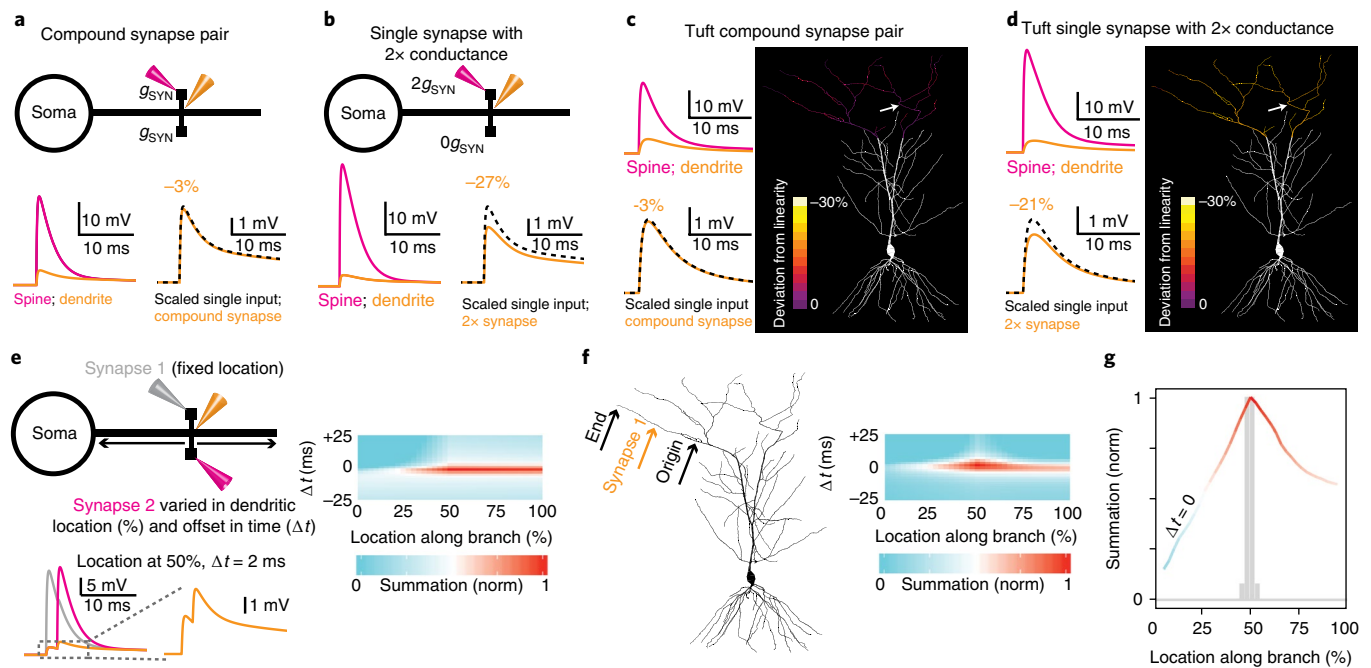
Fig. 8 | Functional effects of compound synaptic connectivity. a, Efficient dendritic depolarization by compound synapses in a passive model. Top, the model morphology containing two synapses in the compound synapse configuration. Bottom left, the voltage change in the spine head (magenta) and in the parent dendrite (orange). Bottom right, the dendritic voltage change from the compound synapse configuration (orange) is almost identical to the scaled single input (dashed black line; −3% deviation from linearity). **b**, Same as in **a**, but for the 2× synapse condition, where the single activated synapse has twice the synaptic conductance. Note the larger synaptic depolarization in the spine head yet smaller peak amplitude of the dendritic depolarization compared to the scaled single input (−27% deviation from linearity). **c**, Efficient tuft dendritic depolarization by compound synapses in a morphologically realistic CA1 model with active dendrites. Left, voltage traces as in **a**, but for inputs onto an active CA1 pyramidal neuron (synapse location denoted with arrow in right diagram). Right, deviation from linearity for compound synapses across the tuft. Instances of supralinear integration by the activation of compound synapses at the most distal portions of terminal branches are depicted as 0% deviation from linearity. **d**, Same as in **c**, but for the 2× synapse condition. Note that instances of supralinear integration at the most distal dendritic sites were not observed in the 2× synapse configuration. **e**, The spatiotemporal clustering inherent to compound synapses maximizes input cooperativity. Top left, the passive model containing a fixed reference synapse (synapse 1) located halfway along the length of the dendrite and a second synapse (synapse 2) whose activation was varied in dendritic location (% branch length) and in time (Δt). Bottom left, example voltage traces from each synapse (gray and magenta) and from the parent dendrite (orange) when synapse 2 is at 50% of the branch length and at Δt = +2 ms. Right, plot of the normalized dendritic peak voltage amplitude across all spatial locations (0–100% of the branch length) and at all times (Δt = +25 ms to −25 ms) for synapse 2. **f**, Left, the location of the fixed reference synapse (synapse 1) within the CA1 dendritic morphology. Right, same as in **e**. **g**, Plot of the synaptic summation for all locations of synapse 2 when Δt = 0, overlaid on the observed distribution of intersynapse distances found between individual synapses in a compound connection (see Fig. 2). See Supplementary Fig. 8 for additional data.

spatial and temporal features associated with these connections provide efficient local depolarization of the parent dendrite.

Compound synapses have been observed previously on SR branches in CA1[28,29,31]. However, several important features differ between these connections in SR and in SLM. We found that the occurrence of compound synapses was rare in SR (~1% of synapses) but markedly more common in SLM (~25% of synapses). Even though our estimates of compound connectivity represent lower bounds (as more remote connections would be missed in our analyses), they suggest a large wiring difference between the two compartments. Second, the morphologies of compound synapses on SR dendrites do not appear different than the population of single synapses on proximal dendrites[28], whereas compound synapses in SLM had distinct features that are associated with greater synaptic strength and efficacy.

The increased prevalence and distinct morphology of tuft compound synapses suggests that they function as a circuit-specific structural mechanism to increase synaptic coupling under conditions where conductance scaling onto single spines is biophysically inefficient. This is consistent with our simulations, wherein compound synapses appear to balance competing features to maximize

local dendritic summation. Compound synapses cluster inputs in space and time to overcome dendritic filtering by optimizing conditions for synaptic charge entry, yet they occur on electrically isolated compartments (i.e., dendritic spines) that minimize sublinear forms of integration. That the spatial and temporal features of compound synapses are optimized to produce maximal local voltage changes suggests that they are able to drive dendritic spikes, either on their own or in conjunction with modest input from other connections located on the same branch. Although our modeling results address the advantages of compound connections when activated in isolation, the benefit of compound connections will be preserved when other excitatory synapses on the same branch are active as well, because the principal problem with restricting very strong synapses to individual spines is that of driving force reduction in the spine head. Such an effect is dependent on a high spine neck resistance, which may be necessary to maintain effective chemical compartmentalization of dendritic spines.

The observation that dendritic spines belonging to a compound connection had correlated synaptic morphologies is consistent with findings from proximal dendritic branches in CA1[28] and with compound synapses found on pyramidal cell dendrites in neocortex[27].

The distance between synapses belonging to a compound connection is within the length that plasticity-related biochemical signals diffuse within the dendritic cable[45]. The lack of morphological correlation between neighboring spines from single connections, however, supports the idea that the shared pre- and postsynaptic activity pattern is a stronger factor in shaping the correlated morphology of compound synapses. A major source of shared postsynaptic activity for SR synapses could be the backpropagating action potential. However, backpropagating action potentials decrease in amplitude and often fail entirely to invade the distal tuft dendrites of CA1 pyramidal cells[46]. Thus, the present findings provide further support for the hypothesis that local dendritic activity can serve as a synaptic plasticity signal in tuft branches, even in the absence of action potential firing in the axon and soma[47–49].

Our findings demonstrated a higher rate of compound synapses in the MEC→CA1 projection than in the LEC→CA1 projections, both of which had a much higher rate of compound synapses than midline thalamus→CA1 projections. Because axon segments can only be followed for short distances in both the TEM and AT volumes, these results do not imply that projections to CA1 with a low fraction of compound synapses fail to form functionally related synaptic clusters. Instead, functional synaptic clusters could arise from different axon collaterals belonging to the same presynaptic neuron or by a wiring mechanism involving the spatial convergence of axons belonging to different neurons that have similar feature selectivity. These wiring strategies may explain the structured connectivity present within the CA3→CA1 circuit targeting proximal dendrites[50] even though compound synapses are rare in this dendritic compartment.

Previous work has demonstrated a strong influence of spatiotemporal synaptic clustering on dendritic integration[16], but the stimulus patterns employed in slice experiments are necessarily artificial and their relevance to the dendritic computations performed in vivo had remained unclear. The present results provide direct evidence supporting the existence of synaptic clustering mechanisms by single axons through the formation of compound synapses. Future experiments should seek to clarify whether sets of compound connections reflect a transfer of information from within a single a stimulus dimension (i.e., whether all compound synapses arise from neurons with spatially modulated firing fields) or instead provide a more flexible wiring mechanism for the binding of disparate representations onto single dendritic branches.

Methods

Methods, including statements of data availability and any associated accession codes and references, are available at https://doi.org/10.1038/s41593-018-0084-6.

References

1. Eichenbaum, H. A cortical-hippocampal system for declarative memory. *Nat. Rev. Neurosci.* **1**, 41–50 (2000).
2. Eichenbaum, H. On the integration of space, time, and memory. *Neuron* **95**, 1007–1018 (2017).
3. Brun, V. H. et al. Place cells and place recognition maintained by direct entorhinal-hippocampal circuitry. *Science* **296**, 2243–2246 (2002).
4. Ito, H. T., Zhang, S. J., Witter, M. P., Moser, E. I. & Moser, M. B. A prefrontal-thalamo-hippocampal circuit for goal-directed spatial navigation. *Nature* **522**, 50–55 (2015).
5. Hargreaves, E. L., Rao, G., Lee, I. & Knierim, J. J. Major dissociation between medial and lateral entorhinal input to dorsal hippocampus. *Science* **308**, 1792–1794 (2005).
6. Jankowski, M. M. et al. Nucleus reuniens of the thalamus contains head direction cells. *Elife* **3**, e03075 (2014).
7. Nakashiba, T., Young, J. Z., McHugh, T. J., Buhl, D. L. & Tonegawa, S. Transgenic inhibition of synaptic transmission reveals role of CA3 output in hippocampal learning. *Science* **319**, 1260–1264 (2008).
8. McHugh, T. J. et al. Dentate gyrus NMDA receptors mediate rapid pattern separation in the hippocampal network. *Science* **317**, 94–99 (2007).
9. Brun, V. H. et al. Impaired spatial representation in CA1 after lesion of direct input from entorhinal cortex. *Neuron* **57**, 290–302 (2008).
10. Golding, N. L., Mickus, T. J., Katz, Y., Kath, W. L. & Spruston, N. Factors mediating powerful voltage attenuation along CA1 pyramidal neuron dendrites. *J. Physiol. (Lond.)* **568**, 69–82 (2005).
11. Stuart, G. & Spruston, N. Determinants of voltage attenuation in neocortical pyramidal neuron dendrites. *J. Neurosci.* **18**, 3501–3510 (1998).
12. Nicholson, D. A. et al. Distance-dependent differences in synapse number and AMPA receptor expression in hippocampal CA1 pyramidal neurons. *Neuron* **50**, 431–442 (2006).
13. Jarsky, T., Roxin, A., Kath, W. L. & Spruston, N. Conditional dendritic spike propagation following distal synaptic activation of hippocampal CA1 pyramidal neurons. *Nat. Neurosci.* **8**, 1667–1676 (2005).
14. Takahashi, H. & Magee, J. C. Pathway interactions and synaptic plasticity in the dendritic tuft regions of CA1 pyramidal neurons. *Neuron* **62**, 102–111 (2009).
15. Stuart, G. J. & Spruston, N. Dendritic integration: 60 years of progress. *Nat. Neurosci.* **18**, 1713–1721 (2015).
16. Losonczy, A. & Magee, J. C. Integrative properties of radial oblique dendrites in hippocampal CA1 pyramidal neurons. *Neuron* **50**, 291–307 (2006).
17. Gasparini, S. & Magee, J. C. State-dependent dendritic computation in hippocampal CA1 pyramidal neurons. *J. Neurosci.* **26**, 2088–2100 (2006).
18. Ariav, G., Polsky, A. & Schiller, J. Submillisecond precision of the input-output transformation function mediated by fast sodium dendritic spikes in basal dendrites of CA1 pyramidal neurons. *J. Neurosci.* **23**, 7750–7758 (2003).
19. Legenstein, R. & Maass, W. Branch-specific plasticity enables self-organization of nonlinear computation in single neurons. *J. Neurosci.* **31**, 10787–10802 (2011).
20. Govindarajan, A., Kelleher, R. J. & Tonegawa, S. A clustered plasticity model of long-term memory engrams. *Nat. Rev. Neurosci.* **7**, 575–583 (2006).
21. Takahashi, N. et al. Locally synchronized synaptic inputs. *Science* **335**, 353–356 (2012).
22. Kleindienst, T., Winnubst, J., Roth-Alpermann, C., Bonhoeffer, T. & Lohmann, C. Activity-dependent clustering of functional synaptic inputs on developing hippocampal dendrites. *Neuron* **72**, 1012–1024 (2011).
23. Wilson, D. E., Whitney, D. E., Scholl, B. & Fitzpatrick, D. Orientation selectivity and the functional clustering of synaptic inputs in primary visual cortex. *Nat. Neurosci.* **19**, 1003–1009 (2016).
24. Iacaruso, M. F., Gasler, I. T. & Hofer, S. B. Synaptic organization of visual space in primary visual cortex. *Nature* **547**, 449–452 (2017).
25. Chen, X., Leischner, U., Rochefort, N. L., Nelken, I. & Konnerth, A. Functional mapping of single spines in cortical neurons in vivo. *Nature* **475**, 501–505 (2011).
26. Chen, T. W. et al. Ultrasensitive fluorescent proteins for imaging neuronal activity. *Nature* **499**, 295–300 (2013).
27. Kasthuri, N. et al. Saturated reconstruction of a volume of neocortex. *Cell* **162**, 648–661 (2015).
28. Bartol, T. M. et al. Nanoconnectomic upper bound on the variability of synaptic plasticity. *Elife* **4**, e10778 (2015).
29. Sorra, K. E. & Harris, K. M. Occurrence and three-dimensional structure of multiple synapses between individual radiatum axons and their target pyramidal cells in hippocampal area CA1. *J. Neurosci.* **13**, 3736–3748 (1993).
30. Knott, G. W., Holtmaat, A., Wilbrecht, L., Welker, E. & Svoboda, K. Spine growth precedes synapse formation in the adult neocortex in vivo. *Nat. Neurosci.* **9**, 1117–1124 (2006).
31. Fiala, J. C., Allwardt, B. & Harris, K. M. Dendritic spines do not split during hippocampal LTP or maturation. *Nat. Neurosci.* **5**, 297–298 (2002).
32. Schmidt, H. et al. Axonal synapse sorting in medial entorhinal cortex. *Nature* **549**, 469–475 (2017).
33. Kasai, H., Matsuzaki, M., Noguchi, J., Yasumatsu, N. & Nakahara, H. Structure-stability-function relationships of dendritic spines. *Trends Neurosci.* **26**, 360–368 (2003).
34. Vlachos, A. et al. Synaptopodin regulates plasticity of dendritic spines in hippocampal neurons. *J. Neurosci.* **29**, 1017–1033 (2009).
35. Holderith, N. et al. Release probability of hippocampal glutamatergic terminals scales with the size of the active zone. *Nat. Neurosci.* **15**, 988–997 (2012).
36. Sheng, Z. H. & Cai, Q. Mitochondrial transport in neurons: impact on synaptic homeostasis and neurodegeneration. *Nat. Rev. Neurosci.* **13**, 77–93 (2012).
37. Wouterlood, F. G., Saldana, E. & Witter, M. P. Projection from the nucleus reuniens thalami to the hippocampal region: light and electron microscopic tracing study in the rat with the anterograde tracer *Phaseolus vulgaris*-leucoagglutinin. *J. Comp. Neurol.* **296**, 179–203 (1990).
38. Micheva, K. D. & Smith, S. J. Array tomography: a new tool for imaging the molecular architecture and ultrastructure of neural circuits. *Neuron* **55**, 25–36 (2007).

39. Rah, J. C. et al. Thalamocortical input onto layer 5 pyramidal neurons measured using quantitative large-scale array tomography. *Front. Neural Circuits* **7**, 177 (2013).

40. Bloss, E. B. et al. Structured dendritic inhibition supports branch-selective integration in CA1 pyramidal cells. *Neuron* **89**, 1016–1030 (2016).

41. Viswanathan, S. et al. High-performance probes for light and electron microscopy. *Nat. Methods* **12**, 568–576 (2015).

42. Tervo, D. G. et al. A designer AAV variant permits efficient retrograde access to projection neurons. *Neuron* **92**, 372–382 (2016).

43. Jasnow, A. M. et al. Thy1-expressing neurons in the basolateral amygdala may mediate fear inhibition. *J. Neurosci.* **33**, 10396–10404 (2013).

44. Harnett, M. T., Makara, J. K., Spruston, N., Kath, W. L. & Magee, J. C. Synaptic amplification by dendritic spines enhances input cooperativity. *Nature* **491**, 599–602 (2012).

45. Harvey, C. D., Yasuda, R., Zhong, H. & Svoboda, K. The spread of Ras activity triggered by activation of a single dendritic spine. *Science* **321**, 136–140 (2008).

46. Spruston, N., Schiller, Y., Stuart, G. & Sakmann, B. Activity-dependent action potential invasion and calcium influx into hippocampal CA1 dendrites. *Science* **268**, 297–300 (1995).

47. Kim, Y., Hsu, C. L., Cembrowski, M. S., Mensh, B. D. & Spruston, N. Dendritic sodium spikes are required for long-term potentiation at distal synapses on hippocampal pyramidal neurons. *Elife* **4**, e06414 (2015).

48. Golding, N. L., Staff, N. P. & Spruston, N. Dendritic spikes as a mechanism for cooperative long-term potentiation. *Nature* **418**, 326–331 (2002).

49. Remy, S. & Spruston, N. Dendritic spikes induce single-burst long-term potentiation. *Proc. Natl. Acad. Sci. USA* **104**, 17192–17197 (2007).

50. Druckmann, S. et al. Structured synaptic connectivity between hippocampal regions. *Neuron* **81**, 629–640 (2014).

Author contributions

E.B.B. conceived the project and designed the experiments in consultation with N.S. E.B.B. performed the experiments and analyzed the experimental data. M.S.C. performed the computer simulations and analyzed the simulation data. B.K. performed the image alignment for all experiments. J.C. built the array tomography microscope and assisted with imaging. R.D.F. advised on tissue preparation and ssTEM imaging. E.B.B. and N.S. wrote the paper with input from all coauthors.

Competing interests

The authors declare no competing interests.

Additional information

Supplementary information is available for this paper at https://doi.org/10.1038/s41593-018-0084-6.

Reprints and permissions information is available at www.nature.com/reprints.

Correspondence and requests for materials should be addressed to N.S.

Publisher's note: Springer Nature remains neutral with regard to jurisdictional claims in published maps and institutional affiliations.

Methods

Mice. All experiments were conducted in accordance with NIH guidelines and with approval of the Janelia Institutional Animal Care and Use Committee (Protocol 14-118). TEM samples were made from a male adult (12 weeks of age) wild-type mouse (*Mus musculus*; C57Bl/6N), and array tomography samples were made from adult (10–14 weeks of age) male Thy-1 YFP line H and Thy-1 GFP line M mice[51]. Mice were housed in a 12-h/12-h light/dark cycle and randomly assigned to experimental conditions on the basis of their availability.

ssTEM sample preparation and imaging. Samples were prepared for ssTEM using a chemical fixation protocol modified from ref. [52]. The brain was chemically fixed via transcardial perfusion with 10 mL of 1% paraformaldehyde in 0.1 M phosphate buffer (PB; pH 7.4) for 1 min followed by 200 mL of 2% paraformaldehyde + 2.5% glutaraldehyde in PB at 7.5 mL/min. Perfusion-fixed 100-μm-thick vibratome slices were incubated in 1% reduced osmium tetroxide (OsO_4 + 1.5% potassium ferrocyanide) for 40 min, 1% OsO_4 for 40 min and 1% uranyl acetate for 40 min, and finally flat embedded in Eponate 12 resin (Ted Pella) and cured at 60 °C for 24 h.

The trimmed block contained most of the stratum radiatum and all of the stratum lacunosum-moleculare of area CA1 (Fig. 1a) and was centered along the proximal–distal axis (approximately 2.4 mm posterior to bregma). Ultrathin 50-nm serial sections were collected onto 1 × 2 mm Synaptek slot grids (Ted Pella), stained with uranyl acetate and Sato's lead[53] and subsequently imaged at 3.8 × 3.8 nm pixel resolution using a Tecnai Spirit BioTWIN TEM. Images were assembled and serial sections were aligned using custom alignment software and transformation algorithms[40] (see Supplementary Video 1). The aligned TEM volume is available at https://neurodata.io/data/bloss18.

TEM reconstructions. Dendritic segments of pyramidal cells (*n* = 20) were traced using RECONSTRUCT[54], while the presynaptic axon for each connection was identified and followed through the volume. Reconstructed dendrites and axons in SR were approximately 80–100 μm from the SR–SLM border, and reconstructed dendrites and axons in SLM were approximately 80–100 μm from the SR–SLM border. A set of aspiny, putative interneuron dendritic segments was also reconstructed in SLM (*n* = 5; from the same area as the SLM pyramidal cell dendrites) along with their presynaptic axonal partners. In addition, a set of excitatory axons (*n* = 43) was traced and their postsynaptic partners were reconstructed (Supplementary Fig. 5). A subset of these excitatory axons (*n* = 20) was randomly identified by the dissector method, whereby two consecutive TEM sections were treated as a reference and look up (and then reversed for the second dissector). In this unbiased analysis, we found that 10 of the 20 traced axons made compound connections within the volume (data not shown).

For the detailed analyses of SLM synaptic ultrastructure, the experimenter was blind to the synapse classification during morphological reconstruction. Reconstructed synapses were included only if they were completely contained in the volume, did not have any missing sections, were not cut parallel to the section plane (rendering it difficult to accurately identify and measure subsynaptic structures) and were not distorted by debris or section folds that might otherwise obscure the ultrastructural features. Spines were first traced using RECONSTRUCT across serial sections and then followed by tracing the PSD and active zone area. The active zone was defined as the presynaptic portion of the membrane that was immediately adjacent to the postsynaptic density. Synaptic vesicles were manually assigned within each terminal, and the distance between the vesicle center and the presynaptic active zone was measured.

The RECONSTRUCT software calculates flat areas of PSDs by summing the individual areas from each section (i.e., length × section thickness) for each synapse; thus PSD area measurements will appear slightly smaller in synapses oriented at smaller angles compared to those oriented directly perpendicular to the sectioning plane. This raises the possibility that the difference in PSD areas between single and compound synapses resulted from disproportionate sampling of spines at more acute angles. If this were the case, then one would expect a markedly weaker correlation between PSD area and spine volume (which is not affected by spine orientation), and we would also expect to see a reduced number of sections contributing to each PSD measurement in single synapses. However, both single and compound synapses showed a near-identical correlation and best-fit regression line slopes between PSD area and spine volume (Fig. 3). Furthermore, we found no difference between single and compound synapse in the number of sections that contributed to the PSD measurement for spines with volumes <0.1 μm³ (single: 3.84 ± 0.14, *n* = 116; compound: 3.6 ± 0.39, *n* = 15; *P* = 0.63), for spines with volumes between 0.1 and 0.2 μm³ (single: 7.22 ± 0.52, *n* = 37; compound: 7.23 ± 0.55, *n* = 22; *P* = 0.92) or for spines with volumes between 0.2 and 0.3 μm³ (single: 9.44 ± 0.59, *n* = 25; compound: 8.73 ± 0.82, *n* = 15; *P* = 0.41).

Intracranial viral injections. In the array tomography experiments, high-titer viral suspension was injected at 10–12 weeks of age as described previously[55]. The titers of each virus were as follows (in genomic copies/mL): AAV2/1-Cre, 2.5 × 10¹³, AAV2/1-FLEX-rev-smRuby_V5, 5.8 × 10¹³, AAV2retro-Cre, 3.7 × 10¹², AAV2/1-FLEX-rev-GFP, 3.5 × 10¹³ and AAV2/1-FLEX-rev-tdTomato, 6.5 × 10¹². To ensure sparse infection of EC neurons, AAV2/1-Cre was diluted 1:100 for the MEC and

LEC experiments shown in Fig. 6. Depending on the experiment, 10–75 nL of viral suspension was injected over 3–5 min. The coordinates were as follows (in mm: posterior relative to bregma, lateral relative to midline, and ventral relative to pial surface): LEC (−4.2, 4.5, 2.5), MEC (−4.5, 3.5, 2.5), midline thalamus (−0.5, 0, 3.7; 0.8, 0, 3.75; −1.1, 0, 3.85; and −1.4, 0, 3.9) and CA1 (−2.3, 1.8 1.5; −2.3, 2.2, 1.5; −2.6, 2.25, 1.65; and −2.6, 2.65, 1.65). At each site, the injection pipette was left in place for 4 min then slowly retracted at a rate of 10 μm/s from the brain. Mice were single housed after surgery and killed 2–4 weeks after injection.

Array tomography sample preparation and imaging. Samples for AT or correlative AT-TEM were prepared exactly as in ref. [40]. Perfusion-fixed coronal mouse slices containing the dorsal CA1 (2.3–2.5 mm posterior from bregma) or BLA (1.3–1.5 mm posterior from bregma) were frozen using a high-pressure freezer (Wohlwend), freeze-substituted, infiltrated with Lowicryl HM20 Monostep resin (Electron Microscopy Sciences) and polymerized for 48 h under UV light (405 nm).

Serial 100-nm sections were collected onto gelatin-coated glass coverslips, processed, and imaged using identical procedures to those in ref.[40]. Synaptic vesicles were labeled by a polyclonal antibody raised against synaptophysin 1 (Synaptic Systems 101004; guinea pig anti-Syn1, 1:2,500, lot 22), GFP- or YFP-expressing pyramidal cells were labeled by a polyclonal antibody against GFP (Abcam 13970; chicken anti-GFP, 1:2500, lot GR236651-13), and afferent axons were labeled by antibodies specific for the V5 epitope tag (Novus MCA1360G, mouse anti-V5, 1:200, lot 0515). Incubation in primary antibodies was followed by incubation in the following fluorescent conjugated secondary antibodies (diluted 1:200): Alexa Fluor 647–conjugated goat anti-guinea pig (106-605-003, Jackson ImmunoResearch, lot 129953), Alexa Fluor 555–conjugated goat anti-mouse (A21424, Invitrogen, lot 1812159) and Alexa Fluor 488–conjugated goat anti-chicken (103-545-155, Jackson ImmunoResearch, lot 130815).

Sixteen-bit images with isotropic voxels (*x*-*y*-*z* dimensions 100 nm × 100 nm × 100 nm) were acquired using a Zeiss AxioObserver wide-field epifluorescence microscope equipped with a 63×, 1.4 NA oil-immersion objective, custom built array acquisition software and an infrared skew-beam autofocus system[39,40]. Syn1 immunoreactivity was used for autofocus, registration and alignment. Images were computationally aligned using identical protocols to those in ref.[40] on the Janelia Research Campus compute cluster (https://github.com/billkarsh/Alignment_Projects).

In AT-TEM experiments, after light-level imaging the Pioloform support film was etched from the glass coverslip with 1.5% hydrofluoric acid, the ribbons were floated onto double distilled H_2O, and Synaptek 1 × 2 mm TEM grids (Ted Pella) were dropped over the ribbons. Slot grids were stained with 5% uranyl acetate in ddH₂0 for 5 min, rinsed in ddH₂0 and then stained with Sato's lead for 1 min. Serial sections were imaged at 3.8 × 3.8 nm pixel resolution using a Tecnai Spirit BioTWIN TEM. AT and TEM images were aligned to each other using the pattern of DAPI fluorescence and the corresponding pattern of nuclear heterochromatin in the TEM images.

Analysis of excitatory afferent connectivity. Antibodies to the synaptic vesicle protein Syn1, which we have extensively validated with correlative AT-TEM experiments[40], were used to isolate putative synaptic connections made by V5-labeled axons onto GFP-or YFP-expressing dendrites. Images from each channel were subjected to an intensity-based threshold and then merged to form a composite image. Putative synapses were defined as the colocalization of dendritic GFP signal, axonal V5 signal and Syn1 signal across serial sections. We have previously validated this synapse identification procedure in correlative AT-TEM experiments, in which 84% of putative synaptic contacts in array tomography were confirmed in the TEM images[40]. Each putative synapse was assigned to a dendrite, and the axon was followed through as many sections as possible. Instances in which the axon could not be followed unambiguously in the area immediately adjacent to the target dendrite were not included in the analysis. Data collection and analysis of afferent projections from AT volumes were not performed blind to the conditions of the experiments.

Computational simulations. For simulations, a stylized ball-and-stick morphology with passive biophysics was used ('passive model'), as well as a morphologically and biophysically realistic CA1 pyramidal neuron[40] ('active model'). All simulations were performed using the NEURON simulation software[56] with a variable time step.

For the passive model, the morphology consisted of a dendrite (50 μm length, 1.0 μm diameter) coupled to a cylinder representing the remainder of the morphology (65 μm length, 65 μm diameter). For illustrative purposes in Fig. 8 and Supplementary Fig. 8, this equivalent cylinder is labeled "soma" and scaled down in size. For both compartments, cm = 1 μF/cm², Ra = 150 Ω cm, g_pas = 1/40,000 S/cm² and e_pas = −65 mV. For the active model, the morphology and active properties were taken from a previous model of a mouse CA1 pyramidal cell[40]. In both the passive and active models, morphologies were augmented with two spines. To facilitate comparison with previous work, we used empirically constrained parameters for spine geometry (neck: 1.58 μm length, 0.077 μm diameter; head: 0.5 μm length, 0.5 μm diameter; spine neck resistance, 500 MΩ[44])

and synaptic properties (passive model: AMPA conductances with $\tau_{1,AMPA} = 0.2\,\text{ms}$, $\tau_{2,AMPA} = 2\,\text{ms}$; active model, both AMPA and NMDA conductances were employed, with $g_{AMPA} = g_{NMDA}$, $\tau_{1,AMPA} = 0.2\,\text{ms}$, $\tau_{2,AMPA} = 2\,\text{ms}$, $\tau_{1,NMDA} = 1\,\text{ms}$, $\tau_{2,NMDA} = 75\,\text{ms}$; in both models, synapse strength was scaled to give ~25 mV depolarization at the spine head[44]). Synapses were placed on spines, with passive and active intrinsic properties of spines matching those of the parent dendrite.

For studying the interaction of compound synaptic input in the passive model, two AMPA synapses were simultaneously activated on two spines located midway across the dendrite compartment. The peak amplitude attained at the site of the parent dendrite was compared to twice the amplitude of a single synapse ('scaled single input') (Fig. 8a), as well the amplitude evoked by a single synapse at twice the peak conductance ('2× synapse') (Fig. 8b) A similar approach was taken in the active model with AMPA and NMDA synapses, with synapses and spines located approximately midway in the tuft (Fig. 8c,d). Deviation from linearity D for compound and 2× synapses was measured by $D = (V_2 - 2V_1)/2V_1$, where V_2 is the peak voltage depolarization the parent dendrite for the two-synapse case (either compound or 2× synapse) and V_1 is the peak voltage depolarization in the parent dendrite for a single input.

For examining the spatiotemporal interaction of synapses in the passive model (Fig. 8e), a spine with an AMPA synapse was added midway across the dendrite ('synapse 1'). Across simulations, a second spine was added at a variable location ('synapse 2'), and the associated AMPA synapse was activated with a variable temporal offset relative to synapse 1. To assess the interaction between these synapses as a function of offset in space and time, the peak depolarization at the associated location on the parent dendrite was monitored. A similar approach was taken with AMPA and NMDA synapses in the active model, with synapse 1 added midway across a terminal tuft branch and synapse 2 varied in space and time across this branch (Fig. 8f,g).

Statistical analyses. No statistical methods were used to predetermine sample sizes, but our sample sizes are similar to those reported in previous publications[12,28,35]. Statistical analyses were performed using GraphPad Prism and R. Datasets were tested for normality using the D'Agostino–Pearson omnibus normality test. Because most datasets were non-normal or had small sample sizes, datasets were analyzed with two-sided non-parametric tests.

Life Sciences Reporting Summary. Further information on experimental design is available in the Life Sciences Reporting Summary.

Code and data availability. Alignment of TEM and AT images was performed using code available at https://github.com/billkarsh/Alignment_Projects. Code for the simulations is available on our laboratory website (http://www.janelia.org/lab/spruston-lab/resources) and in the ModelDB database (http://senselab.med.yale.edu/modeldb/). The raw data that support the findings of this study are available at Figshare (https://doi.org/10.6084/m9.figshare.5550319 and https://doi.org/10.6084/m9.figshare.5700763), also accessible through links from our laboratory website (http://www.janelia.org/lab/spruston-lab/resources). The aligned TEM volume is available at https://neurodata.io/data/bloss18.

References

51. Feng, G. et al. Imaging neuronal subsets in transgenic mice expressing multiple spectral variants of GFP. *Neuron* **28**, 41–51 (2000).
52. Knott, G. W., Holtmaat, A., Trachtenberg, J. T., Svoboda, K. & Welker, E. A protocol for preparing GFP-labeled neurons previously imaged in vivo and in slice preparations for light and electron microscopic analysis. *Nat. Protoc.* **4**, 1145–1156 (2009).
53. Sato, T. A modified method for lead staining of thin sections. *J. Electron Microsc. (Tokyo)* **17**, 158–159 (1968).
54. Fiala, J. C. Reconstruct: a free editor for serial section microscopy. *J. Microsc.* **218**, 52–61 (2005).
55. Royer, S. et al. Control of timing, rate and bursts of hippocampal place cells by dendritic and somatic inhibition. *Nat. Neurosci.* **15**, 769–775 (2012).
56. Hines, M. L. & Carnevale, N. T. The NEURON simulation environment. *Neural Comput.* **9**, 1179–1209 (1997).

nature research

Corresponding author(s): Dr. Nelson Spruston,
manuscript # NN-A60969

☐ Initial submission ☒ Revised version ☐ Final submission

Life Sciences Reporting Summary

Nature Research wishes to improve the reproducibility of the work that we publish. This form is intended for publication with all accepted life science papers and provides structure for consistency and transparency in reporting. Every life science submission will use this form; some list items might not apply to an individual manuscript, but all fields must be completed for clarity.

For further information on the points included in this form, see Reporting Life Sciences Research. For further information on Nature Research policies, including our data availability policy, see Authors & Referees and the Editorial Policy Checklist.

▶ Experimental design

1. **Sample size**

   Describe how sample size was determined.

   > no sample sizes were predetermined with statistical methods. However, our sample sizes were sufficient to detect differences between many of the previously reported features of synapse morphology and axonal connectivity (e.g., spine size or density; see Nicholson et al (2006) and Katz et al (2009)).

2. **Data exclusions**

   Describe any data exclusions.

   > synapses in the TEM volume were excluded from morphological reconstructions if they were not contained fully within the volume, if there were sections missing that contained the synapse, if the synapses were parallel to the plane of sectioning, or if debris or folds obscured the ultrastructural details. synapses in array tomography experiments were excluded if the axons could not be followed through serial sections. A sentence is included in the manuscript that clarifies these criteria in the online Methods.

3. **Replication**

   Describe whether the experimental findings were reliably reproduced.

   > experimental findings from Figure 3 were replicated from a different dataset in Supplementary Figure 5; findings from Figure 6 were replicated in Supplementary Figure 6.

4. **Randomization**

   Describe how samples/organisms/participants were allocated into experimental groups.

   > Typically Thy-1 GFP-M and Thy1 YFP-H mice were littermates and were randomly assigned to experimental groups. This is stated in the online Methods

5. **Blinding**

   Describe whether the investigators were blinded to group allocation during data collection and/or analysis.

   > Investigator was blind to the synapse assignment (i.e., single vs. compound) during morphological reconstructions. Investigator was not blind to the experimental condition (i.e., afferent projection region) for the array tomography experiments.

Note: all studies involving animals and/or human research participants must disclose whether blinding and randomization were used.

6. Statistical parameters

For all figures and tables that use statistical methods, confirm that the following items are present in relevant figure legends (or in the Methods section if additional space is needed).

n/a	Confirmed
☐	☒ The <u>exact sample size</u> (*n*) for each experimental group/condition, given as a discrete number and unit of measurement (animals, litters, cultures, etc.)
☐	☒ A description of how samples were collected, noting whether measurements were taken from distinct samples or whether the same sample was measured repeatedly
☐	☒ A statement indicating how many times each experiment was replicated
☐	☒ The statistical test(s) used and whether they are one- or two-sided (note: only common tests should be described solely by name; more complex techniques should be described in the Methods section)
☐	☒ A description of any assumptions or corrections, such as an adjustment for multiple comparisons
☐	☒ The test results (e.g. *P* values) given as exact values whenever possible and with confidence intervals noted
☐	☒ A clear description of statistics including <u>central tendency</u> (e.g. median, mean) and <u>variation</u> (e.g. standard deviation, interquartile range)
☐	☒ Clearly defined error bars

See the web collection on statistics for biologists for further resources and guidance.

▶ Software

Policy information about availability of computer code

7. Software

Describe the software used to analyze the data in this study.

Dendrites and axon segments were reconstructed in RECONSTRUCT (version 1.1.0.0; https://synapseweb.clm.utexas.edu/software-0). Computational simulations were performed using NEURON software (version 7.3, https://www.neuron.yale.edu/neuron/download) and code has been deposited to the ModelDB database (http://senselab.med.yale.edu/modeldb/). GraphPad Prism (version 6) and R (version 3.4.2) were used for statistical analyses, as stated in the online Methods section. All raw data, simulation code, and analysis code will be deposited onto figshare (images and data), deposited onto neurodata.io (EM volume), deposited onto ModelDB (simulation code). Note the web addresses for these sites are present in the manuscript.

For manuscripts utilizing custom algorithms or software that are central to the paper but not yet described in the published literature, software must be made available to editors and reviewers upon request. We strongly encourage code deposition in a community repository (e.g. GitHub). *Nature Methods* guidance for providing algorithms and software for publication provides further information on this topic.

▶ Materials and reagents

Policy information about availability of materials

8. Materials availability

Indicate whether there are restrictions on availability of unique materials or if these materials are only available for distribution by a for-profit company.

All transgenic animals and viral reagents are commercially available through Jackson Laboratory or addgene, respectively. In addition, we will make the TEM volume publicly available though neurodata.io.

9. Antibodies

Describe the antibodies used and how they were validated for use in the system under study (i.e. assay and species).

Synaptic vesicles were labeled by a polyclonal antibody raised against synaptophysin 1 (Synaptic Systems 101004; guinea pig anti-Syn1, 1:2500, lot# 22), GFP- or YFP-expressing pyramidal cells were labeled by a polyclonal antibody against GFP (Abcam 13970; chicken anti-GFP, 1:2500, lot# GR236651-13), and afferent axons were labeled by antibodies specific for the V5 epitope tag (Novus MCA1360G, mouse anti-V5, 1:200, lot# 0515). Incubation in primary antibodies was followed by incubation in the following fluorescent conjugated secondary antibodies (all diluted 1:200): Alexa Fluor 647–conjugated goat anti-guinea pig (catalog no. 106-605-003, Jackson ImmunoResearch, lot# 129953), Alexa Fluor 555–conjugated goat anti-mouse (catalog no. A21424, Invitrogen, lot# 1812159), and Alexa Fluor 488–conjugated goat anti-chicken (catalog no. 103-545-155, Jackson ImmunoResearch, lot# 130815).

All antibodies have been previously validated with postembed immunogold and correlative array tomography-electron microscopy experiments (Bloss et al, 2016).

10. Eukaryotic cell lines

a. State the source of each eukaryotic cell line used.

> No eukaryotic cell lines were used

b. Describe the method of cell line authentication used.

> No eukaryotic cell lines were used

c. Report whether the cell lines were tested for mycoplasma contamination.

> No eukaryotic cell lines were used

d. If any of the cell lines used are listed in the database of commonly misidentified cell lines maintained by ICLAC, provide a scientific rationale for their use.

> No eukaryotic cell lines were used

▶ Animals and human research participants

Policy information about studies involving animals; when reporting animal research, follow the ARRIVE guidelines

11. Description of research animals

Provide details on animals and/or animal-derived materials used in the study.

> TEM samples were made from a male adult (12 weeks of age) wild-type mouse (C57Bl/6N), and array tomography samples were made from adult male (10-14 weeks of age) Thy-1 YFP line H and Thy-1 GFP line M mice.

Policy information about studies involving human research participants

12. Description of human research participants

Describe the covariate-relevant population characteristics of the human research participants.

> The study did not involve human research participants.